JCB Journal of Cell Biology

TOOLS

# Molecular determinants of ER–Golgi contacts identified through a new FRET–FLIM system

Rossella Venditti[1,2]*, Laura Rita Rega[1]*, Maria Chiara Masone[1], Michele Santoro[1], Elena Polishchuk[1], Daniela Sarnataro[2], Simona Paladino[2], Sabato D'Auria[3], Antonio Varriale[3], Vesa M. Olkkonen[4,5], Giuseppe Di Tullio[1], Roman Polishchuk[1], and Maria Antonietta De Matteis[1,2]

**ER–TGN contact sites (ERTGoCS) have been visualized by electron microscopy, but their location in the crowded perinuclear area has hampered their analysis via optical microscopy as well as their mechanistic study. To overcome these limits we developed a FRET-based approach and screened several candidates to search for molecular determinants of the ERTGoCS. These included the ER membrane proteins VAPA and VAPB and lipid transfer proteins possessing dual (ER and TGN) targeting motifs that have been hypothesized to contribute to the maintenance of ERTGoCS, such as the ceramide transfer protein CERT and several members of the oxysterol binding proteins. We found that VAP proteins, OSBP1, ORP9, and ORP10 are required, with OSBP1 playing a redundant role with ORP9, which does not involve its lipid transfer activity, and ORP10 being required due to its ability to transfer phosphatidylserine to the TGN. Our results indicate that both structural tethers and a proper lipid composition are needed for ERTGoCS integrity.**

## Introduction

Membrane contact sites (MCSs) are sites of close apposition (10–20 nm) between two distinct organelles where the exchange of solutes or lipids occurs between the facing organelles. The ER is involved in forming most (though not all) MCSs with other organelles including mitochondria, the plasma membrane (PM), endosomes, lysosomes, and the Golgi complex (Murley and Nunnari, 2016; Phillips and Voeltz, 2016). These structures have attracted considerable attention in recent years, and several tethering complexes have been identified that mediate the coupling of the apposing organelles (Eisenberg-Bord et al., 2016). The ER–TGN contact sites (ERTGoCS) are the least well defined (De Matteis and Rega, 2015), despite the fact that sites of close apposition between the ER and the last trans cisterna/trans-Golgi network (herein collectively called TGN) have been documented by ultrastructural analysis since the early 1960s (Novikoff, 1964; Rambourg et al., 1979; Ladinsky et al., 1999). This is partly due to the position of the Golgi complex in the crowded perinuclear area that has hampered the analysis of these MCSs by optical microscopy due to the resolution limits of this approach. There is thus a dearth of knowledge regarding fundamental aspects of ERTGoCS such as their frequency, regulation, and composition. These gaps in our knowledge about ERTGoCS, mainly due to methodological limits, have hampered direct studies to address this question. We therefore developed a Förster resonance energy transfer (FRET)-based approach (Grecco and Bastiaens, 2013), which is endowed with the necessary nanoscale resolution power for the study of ERTGoCS.

## Results

### Morphometric analysis of ERTGoCS

We initially performed a morphometric ultrastructural analysis and found that 55–60% of Golgi stacks are engaged in MCSs (defined as areas where the distance between the TGN and the ER membranes is ≤20 nm) with the ER with a distance ranging from 5 to 20 nm (average, 12 nm), a mean length of 176 nm, and a mean occupancy of 24% of the TGN surface area (Fig. 1, A–C). A 3D view of the ERTGoCS using focused ion beam–scanning electron microscopy (FIB-SEM) showed that the ER is closely apposed to the TGN occluding a surface area of up to 0.2 µm$^2$ for each organelle (Fig. 1 D and Video 1).

### ERTGoCS can be visualized by FRET–fluorescence lifetime imaging microscopy (FLIM)

We next developed a FRET-based approach that involves a donor fluorophore molecule (GFP) conjugated to a TGN membrane protein (TGN46) that, when excited, transfers energy to an acceptor fluorophore molecule (mCherry) conjugated

---

[1]Telethon Institute of Genetics and Medicine, Pozzuoli, Italy; [2]Department of Molecular Medicine and Medical Biotechnology, University of Napoli Federico II, Medical School, Naples, Italy; [3]Institute of Food Science, Consiglio Nazionale delle Ricerche, Avellino, Italy; [4]Department of Anatomy, Faculty of Medicine, FI-00014 University of Helsinki, Helsinki, Finland; [5]Minerva Foundation Institute for Medical Research, Biomedicum 2U Helsinki, Helsinki, Finland.

*R. Venditti and L.R. Rega contributed equally to this paper; Correspondence to Maria Antonietta De Matteis: dematteis@tigem.it; Rossella Venditti: venditti@tigem.it.

Rockefeller University Press
J. Cell Biol. 2019 Vol. 218 No. 3 1055–1065

https://doi.org/10.1083/jcb.201812020

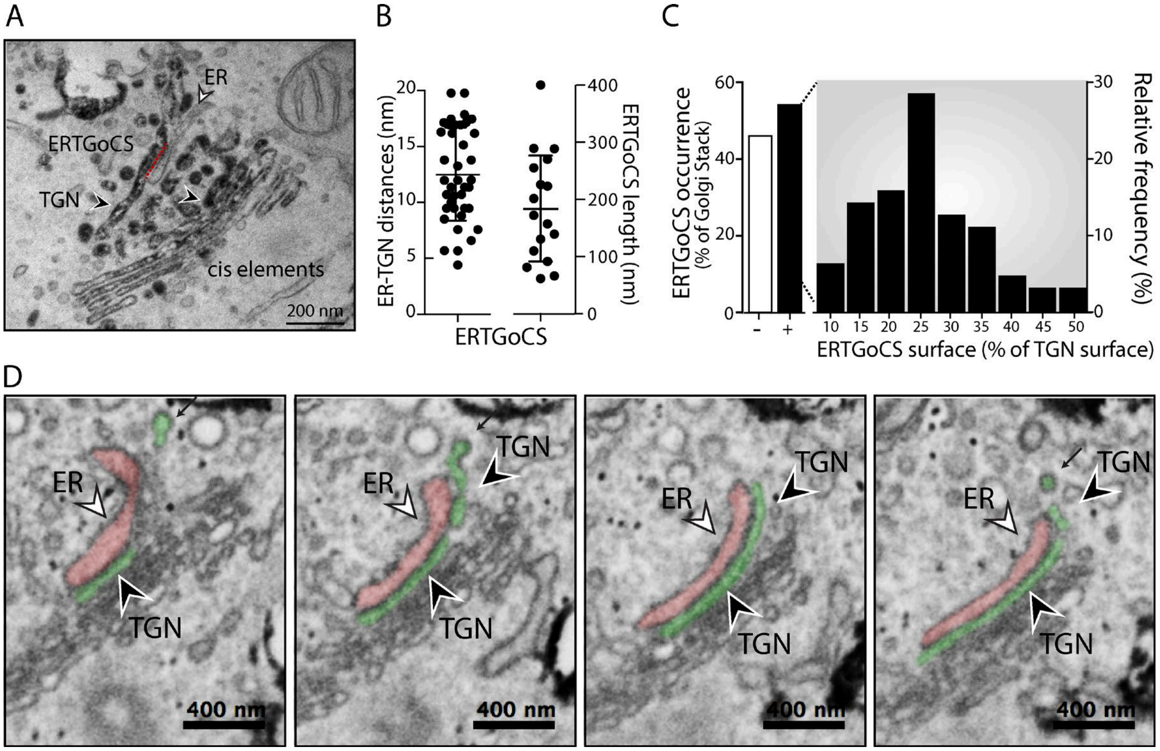

Figure 1. **Morphometric analysis of ERTGoCS. (A)** Electron micrograph showing ER (white arrowhead) closely apposed (red dashed line) to the TGN (black arrowheads) in a HeLa cell expressing TGN46-HRP (visualized by the DAB reaction that produces a dark product in the lumen of the TGN). Golgi cis elements are indicated. **(B)** Measurement of ERTGoCS distance (left; *y* axis) and length (right; *y* axis). Mean ± SD of 40 and 22 Golgi stacks, respectively, representative of three independent experiments. **(C)** Percentage of Golgi stacks negative (white bar) or positive (black bar) for ERTGoCS (left part of graph). In the ERTGoCS-positive Golgi stacks, the frequency distribution of the ERTGoCS surface area was calculated and expressed as a percentage of the total TGN surface (Materials and methods). *n* = 130 Golgi stacks. **(D)** FIB-SEM images of a HepG2 cell. Four images from Video 1 taken every 60 nm representing a total depth of 240 nm. The ER is colored in red and the TGN in green. The small arrow indicates a clathrin-coated profile that identifies the trans pole of the Golgi.

to an ER membrane protein (the C tail of cytochrome b5, Cb5) provided that the two fluorophores are within a distance of 1–10 nm (Fig. 2, A and B; and Materials and methods; Grecco and Bastiaens, 2013). In the presence of FRET phenomenon, the lifetime of the donor becomes shorter, as a consequence of the process of energy transfer to the acceptor molecule. Thus, in our assay we used FLIM of cells expressing TGN46-GFP alone or TGN46-GFP and mCherry-Cb5 at equimolar amounts (Fig. 2 A and Materials and methods). The mean fluorescence lifetime (τ, in nanoseconds) of the TGN46-GFP donor protein was measured by FLIM in defined regions of interest (ROIs; Fig. 2 C and Materials and methods). A clear decrease of the TGN46-GFP mean τ value was detected in cells expressing TGN46-GFP/mCherry-Cb5 compared with cells expressing TGN46-GFP alone or together with cytosolic, free mCherry (Fig. 2, D and E). The FRET efficiency was calculated for each pixel of the ROI, and the spatial FRET distribution was depicted using pseudocolors (Fig. 2 F). A heterogeneous FRET efficiency map was apparent with hot spots likely corresponding to a single ERTGoCS. The FRET signal was abolished by photobleaching the acceptor fluorophore while it was increased using longer helical linkers (Várnai et al., 2007) between the fluorophores and the TGN and ER membrane proteins (Fig. S1, A and B). A FRET–FLIM signal (with an average FRET efficiency of 0.2) was also measured using a different donor fluorophore molecule (Alexa Fluor 430 conjugated to anti-HA antibodies) together with the mCherry acceptor molecule in cells expressing TGN46-HA/mCherry-Cb5 (Fig. S1, C–F).

We tested the FRET-based assay under conditions that have been hypothesized to destabilize ERTGoCS or to artificially induce them (Peretti et al., 2008; Mesmin et al., 2013). To destabilize ERTGoCS, cells were depleted of the VAP proteins (VAPA and VAPB), ER integral membrane proteins that are involved in different classes of contact sites (Murphy and Levine, 2016), by siRNA treatment or by transcription activator-like effector nuclease (TALEN; Dong et al., 2016). Ultrastructural analyses showed the disruption of almost all ERTGoCS, with <10% of the Golgi stacks in VAP-KD cells having an MCS with the ER (Fig. 3 A). Concordantly, the FLIM analysis showed a decreased FRET efficiency of the ER/TGN pair of reporter proteins (with an increase in lifetime of the donor) in VAP-KD and VAP-KO cells as compared with control cells (Fig. 3, B and C; and Fig. S1, E and F). By contrast, the FRET efficiency of the ER/TGN pair of reporter proteins increased significantly (and the lifetime value of the donor decreased) under two independent conditions that stabilize ERTGoCS (Fig. 3, B, D, and E). The first involved the expression of the recombinant protein PH-FFAT (Mesmin et al., 2013) that can bridge the TGN and the ER since it contains a Golgi targeting motif, represented by a PH domain that binds PI4P (the phosphoinositide enriched at the TGN), and an ER targeting motif represented by a FFAT

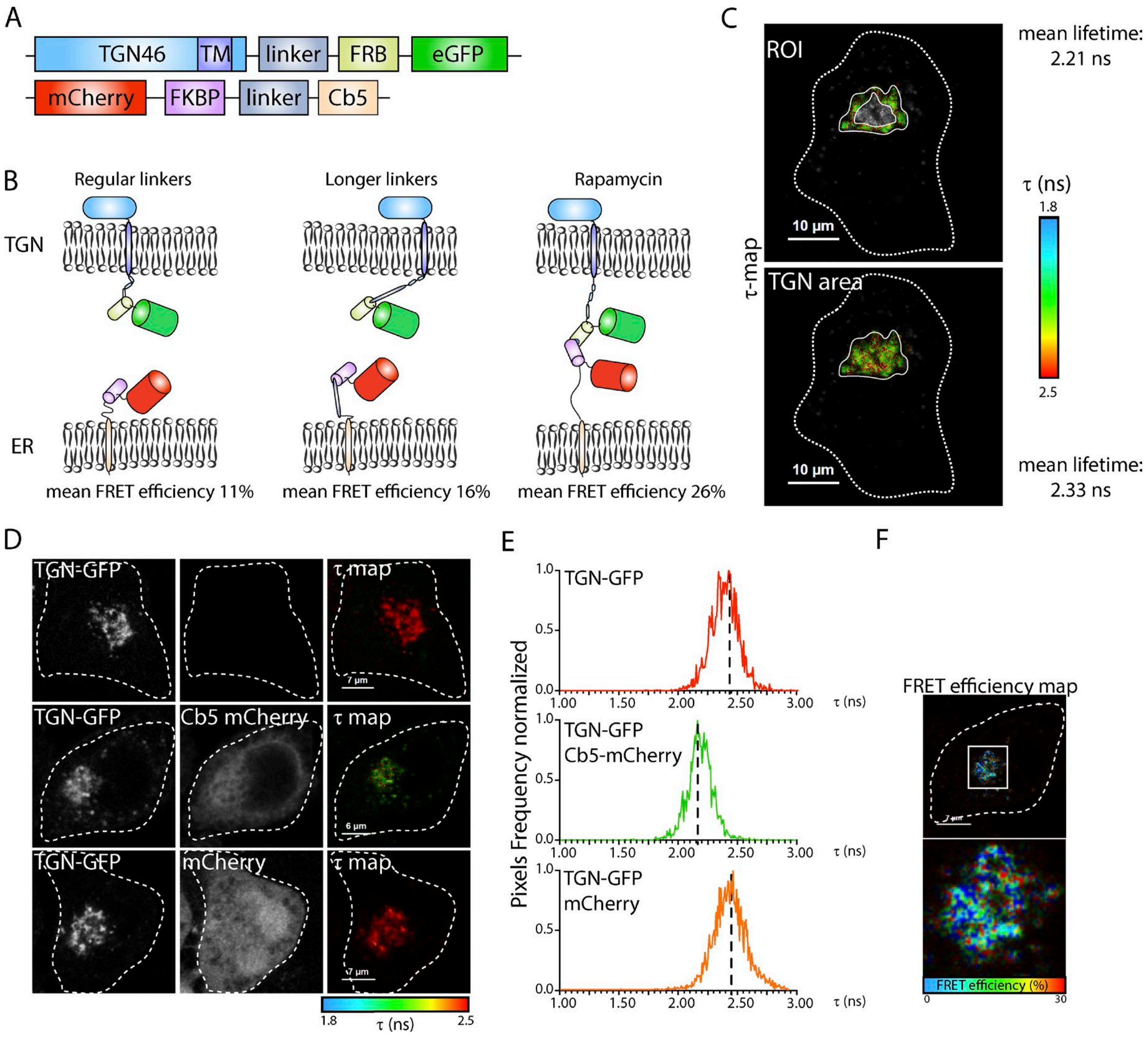

Figure 2. **FRET–FLIM analysis of ERTGoCS. (A)** Schematic representation of the TGN (TGN46-GFP; top construct) and ER (C tail of CytB5, Cb5; bottom construct) membrane reporter proteins used in this study (see Materials and methods for a detailed description of individual domains). **(B)** Graphic representation of the topology of the donor (TGN46-GFP) and the acceptor (mCherry-Cb5) fluorophores at the ERTGoCS under different conditions: left, normal-length linkers (16 amino acids used in the majority of the experiments; Várnai et al., 2007); middle, longer helical linkers (61 amino acids; Várnai et al., 2007); and right, 2 min treatment with 200 nM rapamycin. The mean FRET efficiency measured in the ROI is indicated for each condition. **(C)** The FLIM showing donor (TGN46-GFP) mean lifetime in the presence of the acceptor (mCherry-Cb5) in a defined ROI (top) compared with the whole TGN area (bottom) in cells expressing reporter proteins with normal-length linkers. The τ values are represented by a pseudocolor scale ranging from 1.8 to 2.5 ns. **(D)** FLIM (in color) and immunofluorescence (IF; gray) images of HeLa cells expressing the TGN46-GFP (donor) alone (top), TGN46-GFP and mCherry-Cb5 (donor+acceptor; middle), or TGN46-GFP with free cytosolic mCherry (bottom). The FLIM images show the spatial variation of the mean fluorescence lifetime (τ) of TGN46-GFP: τ values are represented by a pseudocolor scale ranging from 1.8 to 2.5 ns. **(E)** Mean τ value distribution curves of TGN46-GFP (donor) in cells expressing TGN46-GFP alone (top; red line), TGN46-GFP and mCherry-Cb5 (middle; green line), or TGN46-GFP with free mCherry (bottom; orange line). **(F)** The spatial distribution of the FRET efficiency (FRET [%] map) is depicted (color scale ranges from 0 to 30%).

motif that binds the VAP proteins in the ER (Murphy and Levine, 2016; Fig. 3, B and E). The second was the chemically induced dimerization of the TGN46 and Cb5 reporter proteins fused with FRB and FKB domains (Choi et al., 1996) by short treatment with low concentrations of rapamycin (200 nM for 2 min; Fig. 2, A and B; and Fig. 3, B and D).

### ORP10 is required to maintain the ERTGoCS, while OSBP1 and ORP9 have a redundant role

Having validated our FRET–FLIM strategy and with a suitable positive control (i.e., VAP depletion), we performed an siRNA-based search for components of ERTGoCS in cells expressing TGN46-GFP and mCherry-Cb5. We explored the role of proteins that have been proposed as candidate tethering factors between the ER and the Golgi since they possess dual targeting motifs for the two organelles, i.e., a FFAT (FFAT-like motif or putative FFAT motif) and a PI4P-binding PH domain. These proteins included OSBP1 and members of the oxysterol-binding protein-related protein (ORP) family that localize at the Golgi complex (ORP9, ORP10, and ORP11); the ceramide transfer protein CERT; and the FAPP proteins, FAPP1 and FAPP2 (Hanada et al., 2003; D'Angelo et al., 2007; De Matteis et al., 2007; Ngo and Ridgway, 2009; Mikitova and Levine, 2012; Nissilä et al., 2012; Weber-Boyvat et al., 2015; Fig. 4 A). Of note, all the tested proteins, except FAPP1,

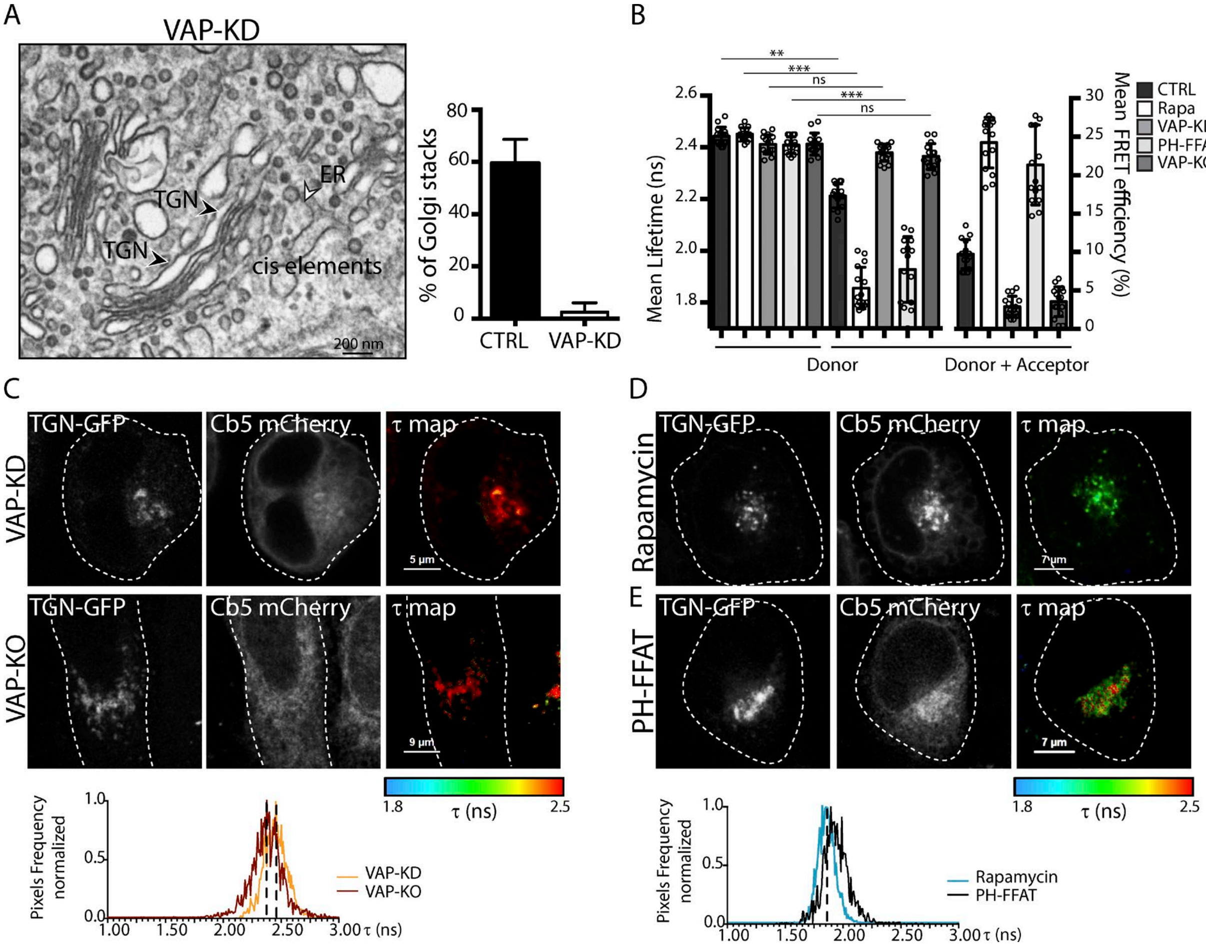

Figure 3. **The VAPs are required to establish/maintain the ERTGoCS. (A)** Electron micrograph of a VAP-KD cell and quantification of ERTGoCS in WT and VAP-KD cells. *n* = 40 Golgi stacks. **(B)** Quantification of average donor lifetime in donor alone or donor+acceptor VAP-KD and VAP-KO HeLa cells, in cells after treatment with rapamycin (2 min, 200 nM), or after transfection with FLAG-tagged PH-FFAT of OSBP1. The corresponding FRET efficiency is shown on the right. *n* = 20; data are means ± SD. **, P < 0.01; ***, P < 0.001; Student's *t* test. **(C–E)** Representative immunofluorescence (IF; gray) and FLIM (in color) images showing donor lifetime in VAP-KD and VAP-KO cells (C), in rapamycin-treated cells (D), and in PH-FFAT–expressing cells (E). The pseudocolor scale representing the τ values of TGN46-GFP is the same as in Fig. 2 D. The graphs show the mean τ value distribution curves of TGN46-GFP under the indicated conditions.

also possess a lipid transfer domain with a distinct lipid specificity. To our surprise, only one (ORP10) out of the entire set of candidates tested affected the stability of the ERTGoCS when depleted. In fact, the mean lifetime of TGN46-GFP in ORP10-depleted cells expressing TGN46-GFP and mCherry-Cb5 was not significantly different from that measured in cells expressing TGN46-GFP alone, and consequently, the FRET efficiency was extremely low in ORP10-depleted cells as compared with control cells (Fig. 4, B and C). We then combined depletion of two candidates at a time, driven by the hypothesis that the depletion of one component might be compensated by another protein with similar activity (Eisenberg-Bord et al., 2016). We found that except for the depletions involving ORP10, only the combined depletion of OSBP1 and ORP9 was able to significantly affect ERTGoCS stability (Fig. 4, B and D). Importantly, the results obtained by FRET–FLIM measurements were validated by ultrastructural and stereological analyses that showed that the only conditions that affected the ERTGoCS organization were ORP10 depletion and the combined depletion of OSBP1 and ORP9 (Fig. 4, E and F; and Fig. S2, A and B).

### ORP10 is required to maintain the ERTGoCS due to its ability to transfer phosphatidylserine (PS)

We next investigated the molecular mechanisms underlying the requirement of the identified hits in sustaining the ERTGoCS and in particular whether this was dependent on their lipid transfer activity. ORP10 associates with microtubules but also with the Golgi complex (Fig. 5 A; Nissilä et al., 2012), and while not possessing a canonical FFAT domain, it can interact with VAPs (Weber-Boyvat et al., 2015; Murphy and Levine, 2016). ORP10 belongs to the ORP subfamily that includes members that can transfer PS (Maeda et al., 2013), such as ORP5 and ORP8 that transfer PS in exchange for PI4P between the ER and the PM (Chung et al., 2015), while ORP10 itself has been shown to bind and extract PS (Maeda et al., 2013). We observed that the residues of the oxysterol-related domain (ORD) of ORP5/ORP8 that are involved in PS/PI4P exchange (Chung et al., 2015) are very well conserved in ORP10 (Fig. 5 B). To investigate whether the requirement for ORP10 in maintaining the ERTGoCS is due to a structural role or to its lipid transfer activity, siRNA-resistant ORP10 was reexpressed in ORP10-depleted cells, both in its WT

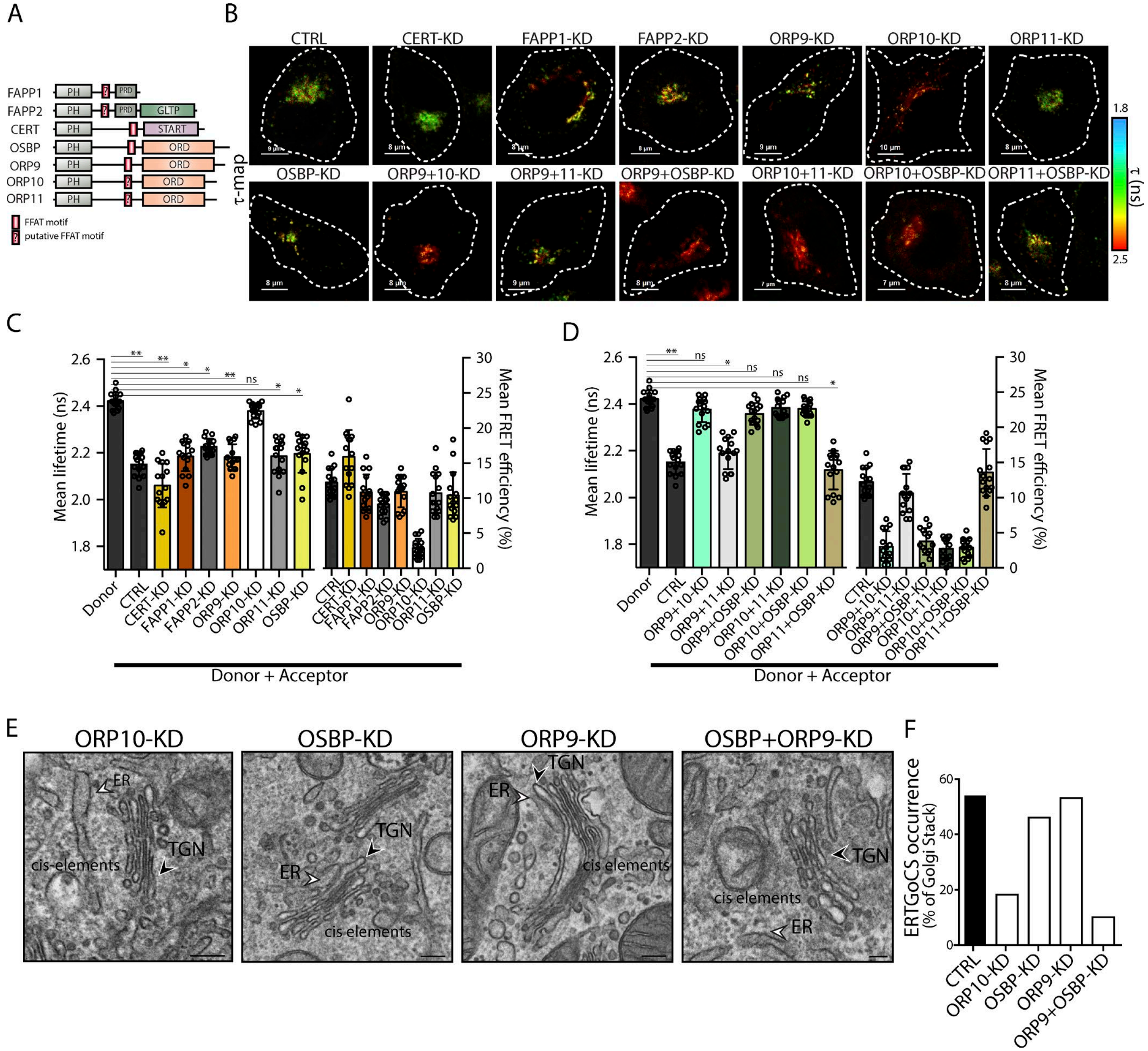

Figure 4. **ORP10 has an essential role, while OSBP and ORP9 play a redundant role in establishing/maintaining the ERTGoCS. (A)** Graphical representation of the candidate proteins analyzed in the siRNA-based screen. The candidates possess a Golgi targeting motif represented by a PI4P-binding PH domain and an ER targeting motif represented by a FFAT motif (OSBP, ORP9, and CERT; Murphy and Levine, 2016) or a putative FFAT-like motif (FAPP2 [Mikitova and Levine, 2012] and ORP10 and ORP11 [Murphy and Levine, 2016]) that mediates the interaction with the VAP ER membrane proteins. FAPP1 possesses two potential FFAT motifs: 165 TFITTLE 171 (if phosphorylated on T165 and T168) and 242 TYSDTDS 248 (if phosphorylated on T242 and S248). **(B)** FLIM images of HeLa cells expressing TGN46-GFP and mCherry-Cb5 (donor+acceptor) transfected with the indicated siRNAs. The τ values are represented by a pseudocolor scale ranging from 1.8 to 2.5. Scale bar, 10 µm. **(C and D)** Quantification of average TGN-GFP lifetime in HeLa cells expressing TGN46-GFP and mCherry-Cb5 (donor+acceptor) and transfected with the indicated single (C) or combined (D) siRNAs. Donor indicates cells transfected with TGN46-GFP alone; CTRL indicates cells transfected with nontargeting siRNAs. The corresponding FRET efficiency is shown on the right. *n* = 20; data are means ± SD. *, $P < 0.05$; **, $P < 0.01$; Student's *t* test. **(E)** Electron micrographs of ORP10-KD, OSBP1-KD, ORP9-KD, and OSBP1+ORP9-KD cells. **(F)** Corresponding quantification of the percentage of Golgi stacks engaged in ERTGoCS (ERTGoCS occurrence). *n* = 20–30 Golgi stacks. Scale bar, 200 nm.

form and in forms where the ORD sites involved in PS (L418D) and PI4P (H535/536A) binding had been mutated (Fig. 5 B). We found that the WT but not the mutant forms of ORP10, which were correctly targeted to the Golgi complex (Fig. 5 C), could reestablish ERTGoCS in ORP10-depleted cells (Fig. 5 D and Fig. S3, A and B), indicating that the lipid transfer activity of ORP10 is required for the stability of these MCSs. PS is synthesized in the ER but is enriched in the PM, the TGN, and endosomes (Leventis and Grinstein, 2010; Fairn et al., 2011), where it is asymmetrically distributed between the bilayer leaflets, being confined to the cytosolic leaflet. Thus, we tested the possibility that ORP10 might be involved in transferring PS from the ER to the cytosolic leaflet of TGN membranes by studying the effect of ORP10 depletion on the subcellular distribution of PS using two distinct genetically

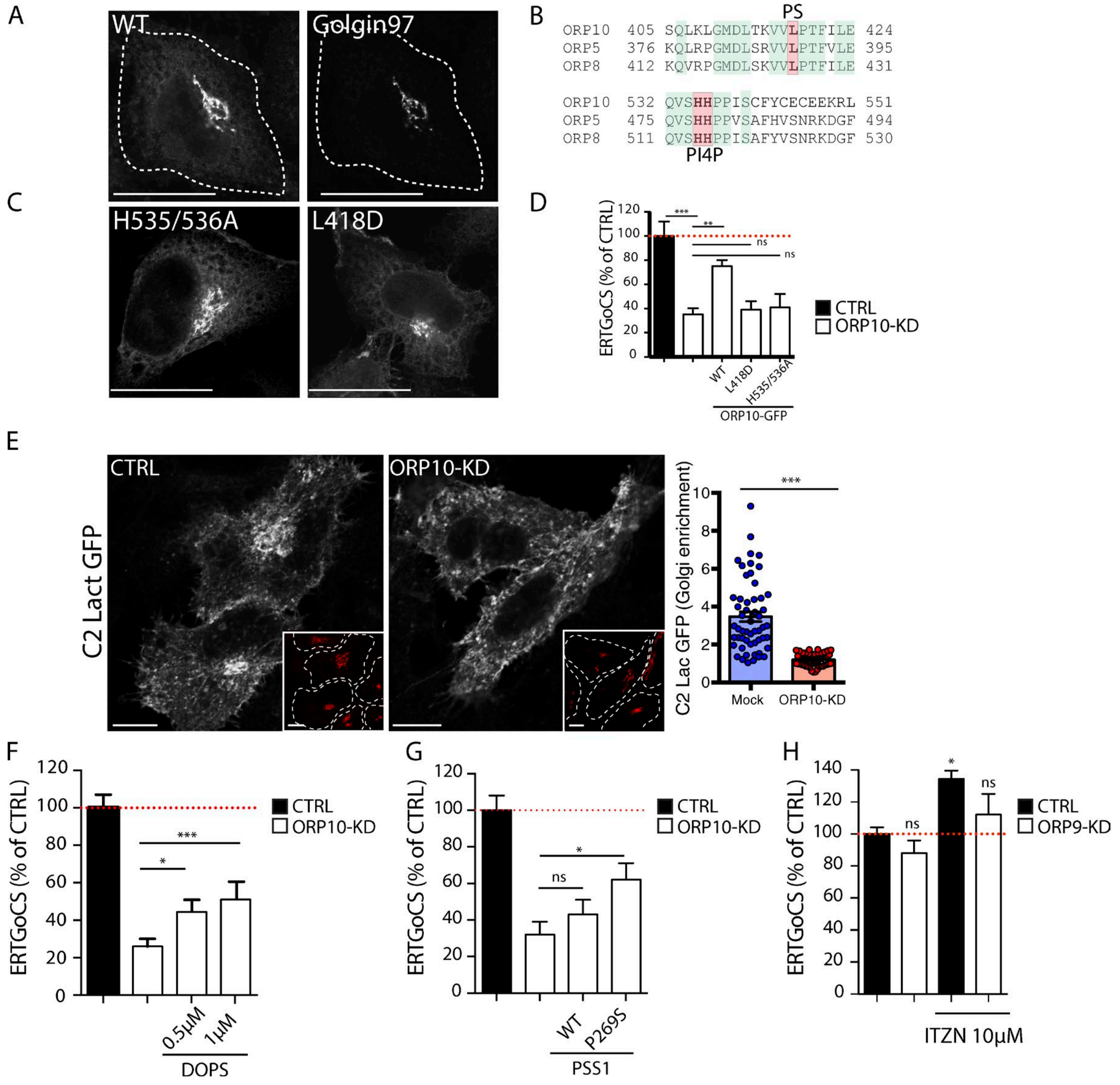

Figure 5. **The integrity of the ERTGoCS requires the PS transfer activity of ORP10. (A)** Subcellular localization of mCherry-tagged WT-ORP10 and of the Golgi marker Golgin-97. Scale bar, 10 µm. **(B)** Residues in ORP5/ORP8 involved in PS/PI4P exchange are conserved in the ORP10 ORD domain. **(C)** Subcellular localization of ORD-domain mutant forms (L418D and H535/536A) of mCherry-tagged ORP10. Scale bar, 10 µm. **(D)** Quantification of ERTGoCS in WT and ORP10-KD cells and in ORP10-KD cells expressing siRNA-resistant GFP-tagged WT-ORP10 or ORD-domain mutant forms of ORP10. The experiment was performed in HeLa cells stably expressing the TGN46-FRB-HA and mCherry-T2A-FKBP-Cb5 reporter proteins as shown in Fig. S3 A and specified in the corresponding legend (see also Materials and methods). Means ± SD of three independent experiments; *n* > 150; **, P < 0.01; ***, P < 0.001; Student's *t* test. **(E)** The PS distribution in control and ORP10-KD cells using the C2 domain of lactadherin (C2-Lact-GFP, a marker for PS). Insets: Golgi marker Golgin-97. Scale bar, 10 µm. Right: Fluorescence intensity ratio of C2-Lact-GFP measured in an equivalent area of the Golgi and the PM in mock and ORP10-KD cells. Data are means ± SD. *n* = 50. ***, P < 0.001; Student's *t* test. **(F and G)** Quantification of ERTGoCS in control cells and in ORP10-KD cells untreated or treated with PS (DOPS; F), or in cells expressing PS synthase 1 (PTDSS1) in its WT and constitutively active (P269S) forms (G). Means ± SD of three independent experiments; *n* > 150. *, P < 0.05; ***, P < 0.001; Student's *t* test. **(H)** Quantification of ERTGoCS in HeLa cells and in ORP9-KD HeLa cells treated with itraconazole. *n* > 150; three independent experiments. Data are means ± SD. *, P < 0.05; ns, not significant with respect to untreated control cells; Student's *t* test.

encoded probes: the PS binding domain of lactadherin (C2 domain; Yeung et al., 2008; Fig. 5 E) and of evectin (PH domain; Uchida et al., 2011; Fig. S3 C). We found that ORP10 depletion induced a decrease in PS at the Golgi as evaluated by the distribution of the two PS probes (Fig. 5 E and Fig. S3 C), which showed a marked reduction of the Golgi pool (but not of the PM pool) in ORP10-KD cells, and by the observation that a lower amount of TGN membranes from ORP10-KD cells was retained on PS-affinity beads as compared with control cells (Fig. S3 D).

Thus, ORP10 is required to safeguard the PS content in the TGN and, at the same time, the ERTGoCS (Fig. 4, A–F; Fig. 5 E; and Fig. S3, C and D), indicating that the lipid composition of the TGN, and in particular its PS content, is of crucial importance for the establishment/maintenance of these structures. Supporting this hypothesis, exogenous supplementation of PS partially restored ERTGoCS in ORP10-depleted cells (Fig. 5 F). Similar results were obtained when the production of PS was boosted through the overexpression of a mutant (P269S) form of PS synthase 1 that is insensitive to product inhibition (Sousa et al., 2014; Sohn et al., 2016; Fig. 5 G and Fig. S3 E).

We addressed the same question (i.e., a structural versus a lipid transfer activity-dependent role in maintaining the ERTGoCS) for OSBP1, which was found to be an obligate partner of ORP9 in maintaining ERTGoCS. To this end, we studied the effect of itraconazole, an inhibitor of OSBP1 lipid exchange activity (Strating et al., 2015), on the stability of the ERTGoCS and found that it had no inhibitory effect either in control cells or in ORP9-KD cells (Fig. 5 H).

## Discussion

Here, we have reported the development of a FRET–FLIM approach to visualize the ERTGoCS in their native form (i.e., in the absence of contact stabilizers) based on the use of a GFP-fused TGN reporter and a cherry-fused ER reporter. While FRET measurements have been previously applied to the study of ER–mitochondria contact sites, they were always under conditions where they had been stabilized by rapamycin-induced dimerization of the organelle reporters (Csordás et al., 2010; Naon et al., 2016).

By coupling FRET–FLIM and EM approaches, we performed the first systematic study aimed at identifying molecular determinants of ERTGoCS. Each approach has complementary pros and cons. The FRET–FLIM approach enables the exploration of multiple conditions, but it provides information that is averaged over the Golgi area without reaching single stack resolution. This is achieved by EM that is endowed with a very limited throughput but provides information on the distribution of ERTGoCS across the different stacks, on their extension and “tightness.” Indeed, by applying rather strict criteria to the definition of ERTGoCS (i.e., sites where the TGN and ER membranes come closer than 20 nm) we show that the distribution of ERTGoCS across the Golgi stacks is not homogeneous, as only a fraction (55%) of Golgi stacks is engaged in ERTGoCS, and the TGN area apposed to the ER in these stacks accounts on average for 24% of the TGN surface. Since the EM provides a snapshot, we cannot presently distinguish between two possible scenarios that could account for this distribution: either all the stacks have the same likelihood to engage in tight contacts with the ER, and at any given time, only 55% exhibit ERTGoCS, or there is only a subset of stacks that has the ability to contact the ER, thus generating heterogeneity among the different Golgi stacks with regard to their closeness to the ER. Additionally, there is also heterogeneity in the width of ERTGoCS, which ranges from 5 to 20 nm, with 40% of them spanning <10 nm.

We have shown that the ERTGoCS require both structural tethers and a proper lipid composition of the TGN. We identified the ER VAP proteins as major determinants of the stability of ERTGoCS since their depletion or ablation (by siRNA or by TALEN) abolished the FRET signal and eliminate the ERTGoCS as evaluated by EM.

The profound destabilizing effect of VAP depletion/ablation can be explained by the role of VAPs as a common ER anchor for the different members of the family of lipid transfer proteins acting at the ERTGoCS. These include OSBP1, ORP9, and ORP10. We have shown that OSBP1 and ORP9, while “using” the ERTGoCS for lipid exchange, can also act as tethers. The higher cellular levels of both OSBP1 and ORP9 (244 and 48 nM, respectively; Hein et al., 2015) and their higher affinity for VAPs (Mikitova and Levine, 2012; Murphy and Levine, 2016) and PI4P (Levine and Munro, 2002) relative to other members of the family may explain why they can play a tethering role. This is also in line with previous reports showing that OSBP1 can tether liposomes in vitro and, when overexpressed (as a WT or transfer-inactive mutant form), induces the wrapping of ER membranes around the Golgi complex (Mesmin et al., 2013). However, our data show that OSBP1 is dispensable for the maintenance of ERTGoCS, since they were unaffected in OSBP1-depleted cells. Instead, the combined depletion of OSBP1 and ORP9 is required to disrupt ERTGoCS demonstrating that they play redundant roles regarding their tethering function. The situation is different for ORP10 that is required to maintain the ERTGoCS due to its ability to transfer PS from the ER to the Golgi, thus indicating that the presence/levels of PS at the TGN are involved in the establishment/maintenance of the contact through mechanisms and effectors that remain to be investigated.

The development of the FRET–FLIM approach to visualize the ERTGoCS paves the way for studies that will lead to the identification of the full repertoire of regulators and constituents of ERTGoCS and to an appraisal of the functional consequences of their destabilization or stabilization. Thanks to this approach we have identified a key role of ERTGoCS in controlling the levels of PI4P at the TGN and in acting as a gatekeeper for the TGN export of selected cargoes (see Venditti et al. in this issue).

## Materials and methods

### Reagents and antibodies

Primary antibodies used in this study were mouse monoclonal anti-HA (Covance), rabbit polyclonal anti-ORP9 (Sigma-Aldrich), rabbit polyclonal anti-ORP10 (Pierce), rabbit polyclonal anti-β actin (Sigma-Aldrich), and sheep polyclonal anti-TGN46 (Serotec). Rabbit polyclonal antibodies against FAPP1, FAPP2 (Godi et al., 2004), VAP-A, VAP-B (Jansen et al., 2011), Golgin-97 (Medina et al., 2015), ORP11, CERT, and OSBP1 were obtained in our laboratories.

The following reagents were kind gifts: TGN46-FRB-HA-CFP and WT and mutant GFP-PTDSS1 from T. Balla (National Institutes of Health, Bethesda, MD), Venus-Cb5 from N. Borgese (Consiglio Nazionale delle Ricerche [CNR], Institute of Neuroscience, Milan, Italy), PH-FFAT-mCherry of OSBP1 from B. Antonny (Centre National de la Recherche Scientifique [CNRS], Institut de Pharmacologie Moléculaire et Cellulaire, Valbonne, France), and TGN38-HRP from D. Cutler (Medical Research Council Laboratory for Molecular Cell Biology, London, UK). The pIRES-neo2, pmCherry-C3, pmCherry-N1, pEGFP-N1, pEGFP-C3, and pEGFP-C1 were purchased from Clontech; p3XFLAG(CMV-14) was purchased from Sigma-Aldrich; pGEX-4T2 was purchased from GE Healthcare; and C2-Lact-GFP (no. 22852) was purchased from AddGene.

Media, serum, and reagents for tissue culture were purchased from Thermo Fisher Scientific. Unless otherwise stated, all chemicals were purchased from Sigma-Aldrich.

### Plasmid construction

All reagents for molecular biology were purchased from New England Biolabs. All mutagenesis was performed by Site-Directed Mutagenesis (Agilent Technologies). The MCS reporter construct TGN46-FRB-HA-GFP-T2A-mCherry-FKBP-Cb5-pIRES-neo2 was generated by sequential subcloning into the pIRES-neo2 vector (see Table S1 for constructs and cloning strategies). Briefly, the ER–membrane reporter Cb5 (17 residues of the transmembrane domain of rat cytochrome b5 [Bulbarelli et al., 2002], cloned inframe downstream of the mCherry-FKBP construct) was cloned into pIRES-neo2 followed by in vitro primer annealing of the T2A peptide coding sequence (Osborn et al., 2005) to produce T2A-mCherry-FKBP-Cb5-IRES-neo2 (note that this cloning procedure resulted in the removal of the AgeI restriction site at the 3′ end, which was reconstituted at the 5′ end of the T2A sequence to allow the sequential cloning of the TGN46 construct). The TGN membrane protein TGN46-FRB-HA-GFP (TGN46 fused with the FKBP12-rapamycin-binding domain FRB) was generated by replacing CFP with GFP in TGN46-FRB-HA-CFP. The resulting TGN46-FRB-HA-GFP construct was used as a template for upstream cloning into T2A-mCherry-FKBP-Cb5-pIRES-neo2. The TGN46-FRB-HA-mCherry-T2A-FKBP-Cb5-pIRES-neo2 plasmid (as above but without GFP) was generated similarly by amplifying TGN46-FRB-HA from TGN46-FRB-HA-GFP and cloning into T2A-mCherry-FKBP-Cb5-pIRES-neo2.

All the cloning strategies adopted for generating the other plasmids used in this study are summarized in Table S1.

### Cell culture, transfection, and RNA interference

HeLa cells were grown in high-glucose (4,500 mg/l) DMEM supplemented with 10% FCS. HeLa WT and HeLa VAP-KO cell lines were a generous gift from P. De Camilli (Yale University School of Medicine, New Haven, CT). VAP-KO cells were generated by a TALEN-based gene-editing approach with TALEN pairs specific to exon 2 of VAPA and VAPB and were cultured as previously described (Dong et al., 2016). HeLa cells stably expressing the MCS pIRES-neo2 reporter vector were isolated as a clone obtained by single cell sorting procedures.

For transfection of DNA plasmids, HeLa cells were transfected using JetPEI (Polyplus) as transfection reagent, and the expression was maintained for 16 h before processing.

siRNA sequences used in this study are listed in Table S2. The HeLa cells were treated for 72 h with Oligofectamine (Life Technologies) for direct transfection. The knockdown efficiency was verified by Western blot analysis and is shown in Fig. S4. Cells treated with identical concentrations of nontargeting siRNAs (D-001810-01-20 and D-001810-02-20; Dharmacon) are referred to as controls.

### Immunofluorescence analysis

HeLa cells were grown on coverslips and fixed with 4% PFA for 10 min, washed three times with PBS, blocked, and permeabilized for 30 min with blocking solution (0.05% saponin, 0.5% BSA, and 50 mM $NH_4Cl$ in PBS) and incubated with primary antibodies diluted in blocking solution for 1 h at RT. Coverslips were washed with PBS and incubated with fluorochrome-conjugated secondary antibodies (Alexa Fluor 488, Alexa Fluor 568, and Alexa Fluor 633) for 1 h at RT. Cells were mounted in Mowiol and imaged with a Plan-Apochromat 63×/1.4 oil objective on a Zeiss LSM800 or LSM880 confocal system equipped with an Electronically Switchable Illumination and Detection (ESID) module and an AiryScan module (for LSM880) and controlled by a Zen blue software. Fluorescence images presented are representative of cells imaged in at least three independent experiments and were processed with Fiji (ImageJ; National Institutes of Health) software. PS distribution (Fig. 5 E) was quantified by performing the fluorescence intensity ratio of C2-Lact-GFP measured in an ROI defining the Golgi area (delimited by the Golgi marker Golgin-97) and in an equivalent area on the PM as described in the corresponding figure legends. Quantification of ER–Golgi contact sites (Fig. 5, D and F–H; and Fig. S3 A) was performed as indicated below and in the corresponding figure legends. Differences among groups were performed using the unpaired Student's *t* test calculated with the GraphPad Prism software. All data were reported as means ± SEM or SD, as indicated in the figure legends.

### FRET–FLIM experiments

For FLIM measurements, HeLa cells were seeded on glass-bottom MatTeK dishes. Cells were transfected with the TGN46-FRB-HA-GFP-T2A-mCherry-FKBP-Cb5-pIRES-neo2 plasmid (Bajar et al., 2016). 16 h after transfection, cells were fixed with 1.87% paraformaldehyde in 1× PBS for 10 min at RT. To reduce autofluorescence, cells were subsequently incubated with 1× PBS supplemented with 50 mM $NH_4Cl$. The imaging was performed in 1× PBS, without any mounting agent. Samples were analyzed the day of preparation without storage at low temperature (i.e., 4°C).

In a parallel set of experiments, we used a different donor fluorophore, Alexa Fluor 430, since the fluorophores Alexa Fluor 430 and mCherry form a favorable Förster donor–acceptor pair with an R0 value (defined as the distance at which 50% of the excited donor molecules transfer energy by FRET) of 6.05 nm (Scalia and Scheffold, 2015). Alexa Fluor 430 was conjugated to anti-HA antibodies (see below) in HeLa cells stably expressing TGN46-FRB-HA-T2A-mCherry-FKBP-Cb5-pIRES-neo2.

Fluorescence lifetime images were acquired using a Zeiss LSM710 (two-photon) confocal microscope, equipped with a FLIM Upgrade kit (Picoquant).

For TGN-GFP detection, the sample was excited using a pulsed femtosecond Ti:Sa laser (Chameleon VISION 2 from Coherent, set at 900 nm) at a fixed repetition rate of 80 MHz. Fluorescence signal was spectrally filtered using a narrowband emission filter (BP-filter 482/35; Chroma). Photons were collected using a single-photon sensitive detector (PMA-Hybrid 40; Picoquant) and timed using a single photon counting module (TimeHarp 260; Picoquant). FLIM data were background subtracted and processed using the pixel-based fitting software SymPhoTime 64 (Picoquant) to calculate the lifetime maps.

We measured the donor lifetime in ROIs, defined as the peripheral regions of the TGN46-GFP positive area (Fig. 2 C) where, in preliminary experiments, we registered that the donor has the lower lifetime suggesting that these were the regions where the donor (i.e., TGN) came closer to the acceptor (i.e., ER). The analysis of lifetime distribution was limited to pixels with >500 total collected photons. Lifetime was determined per single thresholded pixel and used to build histograms of lifetime versus pixel frequency (pixel frequency calculated with reference to total pixels of the ROI). The acquired fluorescence decay curve was deconvoluted with the instrument response function and fitted by a Levenberg–Marquardt least-squares algorithm, using the SymphoTime64 software (PicoQuant). Amplitude-weighted average lifetime was calculated as $\tau = \Sigma(\alpha_i\tau_i)/\Sigma\alpha_i$, where $\alpha_i$ is the amplitude of each lifetime $\tau_i$. FRET–FLIM efficiency was calculated using the equation FRET eff = $1 - (\tau_{DA}/\tau_D)$, where $\tau_{DA}$ is the lifetime of the donor in the presence of the acceptor and $\tau_D$ is the lifetime of the donor without the acceptor (Llères et al., 2017). Validation of the FRET signal in cells expressing TGN46-FRB-HA-GFP-T2A-mCherry-FKBP-Cb5-pIRES-neo2 was performed by photobleaching mCherry-Cb5 in the TGN46-GFP region and then measuring FRET–FLIM.

## Fluorescence labeling of the monoclonal anti-HA antibody

The monoclonal anti-HA antibody was labeled with the reactive fluorescent probe Alexa Fluor 430 NHS Ester (Succinimidyl Ester) purchased from Thermo Fisher Scientific. In brief, the antibody was concentrated and dialyzed in reaction buffer (0.1 M sodium bicarbonate buffer, pH 8.3). 0.2 mg of antibody was mixed with Alexa Fluor 430 with a molar ratio of 12:1 (dye: antibody) in a final volume of 0.125 ml and incubated at RT for 1 h. To remove unreacted fluorescence probe and change buffer, the anti-HA–Alexa Fluor 430 complex was purified using a Sephadex G25 column (GE Healthcare) preequilibrated with 20 mM sodium phosphate, pH 7.4, and 0.1 M NaCl. 50-µl fractions were collected; the absorption spectra between 220 and 600 nm were measured; and the degree of labeling was 4, calculated according to the manufacturer's protocol.

## Rapamycin-induced stabilization of ERTGoCS in cells expressing TGN46-FRB-HA and mCherry-FKBP-Cb5

As shown in Fig. 3 D, brief treatment with low concentrations of rapamycin (2 min, 200 nM) of HeLa cells expressing TGN46-FRB-HA-GFP and mCherry-FKBP-Cb5 induced a marked decrease of TGN-GFP lifetime, indicating a stabilization of ERTGoCS.

We observed that as a consequence of ERTGoCS stabilization, this rapamycin treatment also induced a peri-Golgi clustering of the ER reporter protein Cb5 (Fig. 3 D and Fig. S3 A). Importantly, the perinuclear clustering induced by 2-min rapamycin treatment was largely prevented in ORP10-depleted cells (Fig. S3 A), indicating that under these mild treatment conditions, rapamycin was stabilizing preexisting physiological ERTGoCS and not inducing artificial tethering between the TGN and the ER. However, the perinuclear clustering of Cb5 could be restored in ORP10-depleted cells by reexpressing an siRNA-resistant form of ORP10 (Fig. 5 D and Fig. S3 A) or by elevating PS levels (Fig. 5, F and G). To follow the rapamycin-induced stabilization of ERTGoCS, HeLa cells expressing TGN46-FRB-HA-GFP-mCherry-FKBP-Cb5 and treated with the indicated siRNAs were pretreated with 50 µg/ml cycloheximide for 30 min and then treated with 200 nM rapamycin at 37°C for the indicated time points, followed by paraformaldehyde fixation. Both the cycloheximide and the rapamycin treatments were performed in complete growth medium at 37°C. Cells were then stained with the anti-HA antibody (to verify TGN46 expression) and with a Golgi marker (Golgin-97 to check the overall status of the cells). 15–20 individual fields were imaged (for a total of 150–200 cells) and analyzed to assess mCherry-Cb5 localization. P values were calculated on the basis of mean values from at least three independent experiments.

## EM and stereological analysis

The EM samples were prepared as previously described (D'Angelo et al., 2007). Briefly, cells were fixed by adding to the culture medium the same volume of a mixture of PHEM buffer (10 mM EGTA, 2 mM $MgCl_2$, 60 mM Pipes, and 25 mM Hepes, pH 6.9), 4% PFA, and 2% glutaraldehyde for 2 h and then stored in storage solution (PHEM buffer and 0.5% PFA) overnight. After washing with 0.15 M glycine buffer in PBS, the cells were scraped and pelleted by centrifugation, embedded in 10% gelatin, cooled on ice, and cut into 0.5-mm blocks. The blocks were infused with 2.3 M sucrose and trimmed with an ultramicrotome (Ultracut R; Leica) at −120°C using a dry diamond knife.

For the quantification of ERTGoCS, only the Golgi stacks in which both the cis and trans elements were clearly distinguishable were considered. In one set of experiments, ERTGoCS were quantified in HeLa cells expressing TGN38 conjugated with HRP in which the TGN could be identified by the dark DAB reaction product (Fig. 1 A). The membranes of the ER were identified by the presence of associated ribosomes.

The number of ERTGoCS was quantified using the software of a Philips Tecnai-12 electron microscope, considering a contact site to be a region where ER and TGN membranes come closer than 20 nm for a tract of at least 60 nm. We measured both the contact site length, which spanned from 61 to 290 nm, and its width, expressed as the mean distance of three segments of the contact.

To measure the percentage of the TGN surface in contact with the ER, the TGN surface was estimated by using a stereological approach (grid intersection counting; Mayhew, 1979; Ferguson et al., 2017). Briefly, a grid made of arrays of 50 × 50-nm squares was superimposed on each image, and the total intersections of ERTGoCS (areas were the distance between TGN and the ER membranes is ≤20 nm) and the total intersections of TGN membranes with the test square edges were counted. The ratio between the two counts is an estimation of the percentage of TGN surface engaged in MCSs with the ER.

At the same time, we measured the ratio between the TGN surface (calculated as detailed above) and the area of the cytoplasm (expressed in square micrometers) to assess whether the total TGN area was affected in any of the analyzed conditions. We found that this ratio remained constant and similar to the control in all the analyzed conditions.

## FIB-SEM tomography

The 3D organization of ERTGoCS was analyzed in a Crossbeam 550 FIB-SEM system operating under SmartSEM and Atlas3D software (Zeiss). Epon-embedded cell pellets were first investigated by TEM to assess the quality and contrast of the specimens. Resin blocks were then mounted on SEM specimen stubs and coated with a thin layer of platinum. Trimmed surfaces of

Epon blocks were used to find the cells and then to obtain tomographic datasets with the slice and view technique. Slicing was performed using the focused Ga ion beam with each step removing 15 nm of the Epon-embedded material. The SEM images were recorded with an EsB detector at 5 × 5-nm pixel size. The contrast of the images was inverted so that they appeared like a conventional brightfield TEM image. Serial FIB-SEM images were imported into open-source ImageJ software to generate QuickTime movies and annotations (Video 1).

### PS-affinity isolation of subcellular fractions

The HeLa cells (control and ORP10-KD cells) were broken in hypotonic buffer (10 mM Tris HCl, pH 7.4, and 1.5 mM $MgCl_2$) containing 1 mM DTT and protease inhibitors using a cell cracker apparatus (at a clearance of 8 µm). Cell lysates were diluted 1:2 in incubation buffer (final concentration, 40 mM Tris HCl, pH 7.4, 80 mM NaCl, 70 mM KCl, 250 mM sorbitol, 1 mM EDTA, 1 mM $MgCl_2$, 1 mM DTT, and protease inhibitors) and clarified by centrifugation at 1,500 ×*g* for 10 min at 4°C. The supernatants (1.6 mg $ml^{-1}$) were preincubated with 0.1 µM GST-LacC2 domain or with 0.1 µM GST for 5 h at 4°C and then incubated with Glutathione Magnetic Agarose Beads (Pierce; 25 µl beads for 500 µl cell lysate) for 1 h at 4°C. After six washes with incubation buffer (without sorbitol and with 0.0005% Tween 20) the beads were treated with Laemmli sample buffer, and the eluted fractions were analyzed by SDS-PAGE and Western blot with antibodies against a TGN marker (TGN46). The ratio between the TGN46 signal in the eluted fractions and that in the input was calculated in control and ORP10-KD samples, and the results were expressed as a percentage of the control.

### Online supplemental material

Fig. S1 shows the validation of the FRET–FLIM approach to visualize ERTGoCS. Fig. S2 shows the morphometric analysis of ERTGoCS in cells depleted of lipid transfer proteins found to be dispensable for ERTGoCS integrity by FRET–FLIM. Fig. S3 shows how ORP10 controls PS levels at the TGN. Fig. S4 shows the effect of siRNAs used in the study on target protein levels. Table S1 shows a list of primers and cloning strategies used in this study. Table S2 shows the list of siRNA sequences used in this study. Video 1 shows the FIB-SEM analysis of ERTGoCS.

## Acknowledgments

We thank all the colleagues who kindly provided the reagents listed in Materials and methods and Francesca Zappa, Leopoldo Staiano, Sangram Raut, Zygmunt Gryczynski, Voelker Buschmann, and Cathal Wilson for helpful discussion.

M.A. De Matteis acknowledges the support of Telethon grant TGM11CB1, Associazione Italiana per la Ricerca sul Cancro grant IG2013_14761, and European Research Council Advanced Investigator grant 670881 (SYSMET). V.M. Olkkonen acknowledges the support of the Academy of Finland (grant 285223) and the Sigrid Juselius Foundation. R. Venditti acknowledges the University of Naples Federico II (Bando STAR Linea1-20187 grant).

The authors declare no competing financial interests.

Author contributions: R. Venditti, L.R. Rega, and M.A. De Matteis conceived the work. R. Venditti, L.R. Rega, and M.C. Masone planned and analyzed most of the experiments. E. Polishchuk and R. Polishchuk performed EM and FIB-SEM analyses. G. Di Tullio and M. Santoro provided technical support. D. Sarnataro and S. Paladino performed the initial FRET analysis. V.M. Olkkonen provided ORP10 reagents and discussed the ORP10 relevant data. S. D'Auria and A. Varriale contributed to the FRET studies and labeled the anti-HA antibody. M.A. De Matteis conceptualized the work and strategy and wrote the manuscript together with R. Venditti and M.C. Masone.

Submitted: 5 December 2018
Revised: 14 December 2018
Accepted: 18 December 2018

## References

Bajar, B.T., E.S. Wang, S. Zhang, M.Z. Lin, and J. Chu. 2016. A guide to fluorescent protein FRET pairs. *Sensors (Basel)*. 16:E1488. https://doi.org/10.3390/s16091488

Bulbarelli, A., T. Sprocati, M. Barberi, E. Pedrazzini, and N. Borgese. 2002. Trafficking of tail-anchored proteins: Transport from the endoplasmic reticulum to the plasma membrane and sorting between surface domains in polarised epithelial cells. *J. Cell Sci.* 115:1689–1702.

Choi, J., J. Chen, S.L. Schreiber, and J. Clardy. 1996. Structure of the FKBP12-rapamycin complex interacting with the binding domain of human FRAP. *Science*. 273:239–242. https://doi.org/10.1126/science.273.5272.239

Chung, J., F. Torta, K. Masai, L. Lucast, H. Czapla, L.B. Tanner, P. Narayanaswamy, M.R. Wenk, F. Nakatsu, and P. De Camilli. 2015. PI4P/phosphatidylserine countertransport at ORP5- and ORP8-mediated ER-plasma membrane contacts. *Science*. 349:428–432. https://doi.org/10.1126/science.aab1370

Csordás, G., P. Várnai, T. Golenár, S. Roy, G. Purkins, T.G. Schneider, T. Balla, and G. Hajnóczky. 2010. Imaging interorganelle contacts and local calcium dynamics at the ER-mitochondrial interface. *Mol. Cell*. 39:121–132. https://doi.org/10.1016/j.molcel.2010.06.029

D'Angelo, G., E. Polishchuk, G. Di Tullio, M. Santoro, A. Di Campli, A. Godi, G. West, J. Bielawski, C.-C. Chuang, A.C. van der Spoel, et al. 2007. Glycosphingolipid synthesis requires FAPP2 transfer of glucosylceramide. *Nature*. 449:62–67. https://doi.org/10.1038/nature06097

De Matteis, M.A., and L.R. Rega. 2015. Endoplasmic reticulum-Golgi complex membrane contact sites. *Curr. Opin. Cell Biol.* 35:43–50. https://doi.org/10.1016/j.ceb.2015.04.001

De Matteis, M.A., A. Di Campli, and G. D'Angelo. 2007. Lipid-transfer proteins in membrane trafficking at the Golgi complex. *Biochim. Biophys. Acta*. 1771:761–768. https://doi.org/10.1016/j.bbalip.2007.04.004

Dong, R., Y. Saheki, S. Swarup, L. Lucast, J.W. Harper, and P. De Camilli. 2016. Endosome-ER contacts control actin nucleation and retromer function through VAP-dependent regulation of PI4P. *Cell*. 166:408–423. https://doi.org/10.1016/j.cell.2016.06.037

Eisenberg-Bord, M., N. Shai, M. Schuldiner, and M. Bohnert. 2016. A tether is a tether is a tether: Tethering at membrane contact sites. *Dev. Cell*. 39:395–409. https://doi.org/10.1016/j.devcel.2016.10.022

Fairn, G.D., N.L. Schieber, N. Ariotti, S. Murphy, L. Kuerschner, R.I. Webb, S. Grinstein, and R.G. Parton. 2011. High-resolution mapping reveals topologically distinct cellular pools of phosphatidylserine. *J. Cell Biol.* 194:257–275. https://doi.org/10.1083/jcb.201012028

Ferguson, S., A.M. Steyer, T.M. Mayhew, Y. Schwab, and J.M. Lucocq. 2017. Quantifying Golgi structure using EM: Combining volume-SEM and stereology for higher throughput. *Histochem. Cell Biol.* 147:653–669. https://doi.org/10.1007/s00418-017-1564-6

Godi, A., A. Di Campli, A. Konstantakopoulos, G. Di Tullio, D.R. Alessi, G.S. Kular, T. Daniele, P. Marra, J.M. Lucocq, and M.A. De Matteis. 2004. FAPPs control Golgi-to-cell-surface membrane traffic by binding to ARF and PtdIns(4)P. *Nat. Cell Biol.* 6:393–404. https://doi.org/10.1038/ncb1119

Grecco, H.E., and P.I.H. Bastiaens. 2013. Quantifying cellular dynamics by fluorescence resonance energy transfer (FRET) microscopy. *Curr. Protoc. Neurosci*. Chapter 5:Unit 5.22.

Hanada, K., K. Kumagai, S. Yasuda, Y. Miura, M. Kawano, M. Fukasawa, and M. Nishijima. 2003. Molecular machinery for non-vesicular trafficking of ceramide. *Nature.* 426:803–809. https://doi.org/10.1038/nature02188

Hein, M.Y., N.C. Hubner, I. Poser, J. Cox, N. Nagaraj, Y. Toyoda, I.A. Gak, I. Weisswange, J. Mansfeld, F. Buchholz, et al. 2015. A human interactome in three quantitative dimensions organized by stoichiometries and abundances. *Cell.* 163:712–723. https://doi.org/10.1016/j.cell.2015.09.053

Jansen, M., Y. Ohsaki, L.R. Rega, R. Bittman, V.M. Olkkonen, and E. Ikonen. 2011. Role of ORPs in sterol transport from plasma membrane to ER and lipid droplets in mammalian cells. *Traffic.* 12:218–231. https://doi.org/10.1111/j.1600-0854.2010.01142.x

Ladinsky, M.S., D.N. Mastronarde, J.R. McIntosh, K.E. Howell, and L.A. Staehelin. 1999. Golgi structure in three dimensions: Functional insights from the normal rat kidney cell. *J. Cell Biol.* 144:1135–1149. https://doi.org/10.1083/jcb.144.6.1135

Leventis, P.A., and S. Grinstein. 2010. The distribution and function of phosphatidylserine in cellular membranes. *Annu. Rev. Biophys.* 39:407–427. https://doi.org/10.1146/annurev.biophys.093008.131234

Levine, T.P., and S. Munro. 2002. Targeting of Golgi-specific pleckstrin homology domains involves both PtdIns 4-kinase-dependent and -independent components. *Curr. Biol.* 12:695–704. https://doi.org/10.1016/S0960-9822(02)00779-0

Llères, D., A.P. Bailly, A. Perrin, D.G. Norman, D.P. Xirodimas, and R. Feil. 2017. Quantitative FLIM-FRET microscopy to monitor nanoscale chromatin compaction in vivo reveals structural roles of condensin complexes. *Cell Reports.* 18:1791–1803. https://doi.org/10.1016/j.celrep.2017.01.043

Maeda, K., K. Anand, A. Chiapparino, A. Kumar, M. Poletto, M. Kaksonen, and A.C. Gavin. 2013. Interactome map uncovers phosphatidylserine transport by oxysterol-binding proteins. *Nature.* 501:257–261. https://doi.org/10.1038/nature12430

Mayhew, T.M. 1979. Basic stereological relationships for quantitative microscopical anatomy—A simple systematic approach. *J. Anat.* 129:95–105.

Medina, D.L., S. Di Paola, I. Peluso, A. Armani, D. De Stefani, R. Venditti, S. Montefusco, A. Scotto-Rosato, C. Prezioso, A. Forrester, et al. 2015. Lysosomal calcium signalling regulates autophagy through calcineurin and TFEB. *Nat. Cell Biol.* 17:288–299. https://doi.org/10.1038/ncb3114

Mesmin, B., J. Bigay, J. Moser von Filseck, S. Lacas-Gervais, G. Drin, and B. Antonny. 2013. A four-step cycle driven by PI(4)P hydrolysis directs sterol/PI(4)P exchange by the ER-Golgi tether OSBP. *Cell.* 155:830–843. https://doi.org/10.1016/j.cell.2013.09.056

Mikitova, V., and T.P. Levine. 2012. Analysis of the key elements of FFAT-like motifs identifies new proteins that potentially bind VAP on the ER, including two AKAPs and FAPP2. *PLoS One.* 7:e30455. https://doi.org/10.1371/journal.pone.0030455

Murley, A., and J. Nunnari. 2016. The emerging network of mitochondria-organelle contacts. *Mol. Cell.* 61:648–653. https://doi.org/10.1016/j.molcel.2016.01.031

Murphy, S.E., and T.P. Levine. 2016. VAP, a versatile access point for the endoplasmic reticulum: Review and analysis of FFAT-like motifs in the VAPome. *Biochim. Biophys. Acta.* 1861(8 Pt B):952–961. https://doi.org/10.1016/j.bbalip.2016.02.009

Naon, D., M. Zaninello, M. Giacomello, T. Varanita, F. Grespi, S. Lakshminaranayan, A. Serafini, M. Semenzato, S. Herkenne, M.I. Hernández-Alvarez, et al. 2016. Critical reappraisal confirms that Mitofusin 2 is an endoplasmic reticulum-mitochondria tether. *Proc. Natl. Acad. Sci. USA.* 113:11249–11254. https://doi.org/10.1073/pnas.1606786113

Ngo, M., and N.D. Ridgway. 2009. Oxysterol binding protein-related Protein 9 (ORP9) is a cholesterol transfer protein that regulates Golgi structure and function. *Mol. Biol. Cell.* 20:1388–1399. https://doi.org/10.1091/mbc.e08-09-0905

Nissilä, E., Y. Ohsaki, M. Weber-Boyvat, J. Perttilä, E. Ikonen, and V.M. Olkkonen. 2012. ORP10, a cholesterol binding protein associated with microtubules, regulates apolipoprotein B-100 secretion. *Biochim. Biophys. Acta.* 1821:1472–1484. https://doi.org/10.1016/j.bbalip.2012.08.004

Novikoff, A.B. 1964. GERL, its form and function in neurons of rat spinal ganglia. *Biol. Bull.* 127:358.

Osborn, M.J., A. Panoskaltsis-Mortari, R.T. McElmurry, S.K. Bell, D.A.A. Vignali, M.D. Ryan, A.C. Wilber, R.S. McIvor, J. Tolar, and B.R. Blazar. 2005. A picornaviral 2A-like sequence-based tricistronic vector allowing for high-level therapeutic gene expression coupled to a dual-reporter system. *Mol. Ther.* 12:569–574. https://doi.org/10.1016/j.ymthe.2005.04.013

Peretti, D., N. Dahan, E. Shimoni, K. Hirschberg, and S. Lev. 2008. Coordinated lipid transfer between the endoplasmic reticulum and the Golgi complex requires the VAP proteins and is essential for Golgi-mediated transport. *Mol. Biol. Cell.* 19:3871–3884. https://doi.org/10.1091/mbc.e08-05-0498

Phillips, M.J., and G.K. Voeltz. 2016. Structure and function of ER membrane contact sites with other organelles. *Nat. Rev. Mol. Cell Biol.* 17:69–82. https://doi.org/10.1038/nrm.2015.8

Rambourg, A., Y. Clermont, and L. Hermo. 1979. Three-dimensional architecture of the Golgi apparatus in Sertoli cells of the rat. *Am. J. Anat.* 154:455–475. https://doi.org/10.1002/aja.1001540402

Scalia, G., and F. Scheffold. 2015. Lifetime of fluorescent dye molecules in dense aqueous suspensions of polystyrene nanoparticles. *Opt. Express.* 23:29342–29352. https://doi.org/10.1364/OE.23.029342

Sohn, M., P. Ivanova, H.A. Brown, D.J. Toth, P. Varnai, Y.J. Kim, and T. Balla. 2016. Lenz-Majewski mutations in PTDSS1 affect phosphatidylinositol 4-phosphate metabolism at ER-PM and ER-Golgi junctions. *Proc. Natl. Acad. Sci. USA.* 113:4314–4319. https://doi.org/10.1073/pnas.1525719113

Sousa, S.B., D. Jenkins, E. Chanudet, G. Tasseva, M. Ishida, G. Anderson, J. Docker, M. Ryten, J. Sa, J.M. Saraiva, et al. 2014. Gain-of-function mutations in the phosphatidylserine synthase 1 (PTDSS1) gene cause Lenz-Majewski syndrome. *Nat. Genet.* 46:70–76. https://doi.org/10.1038/ng.2829

Strating, J.R.P.M., L. van der Linden, L. Albulescu, J. Bigay, M. Arita, L. Delang, P. Leyssen, H.M. van der Schaar, K.H.W. Lanke, H.J. Thibaut, et al. 2015. Itraconazole inhibits enterovirus replication by targeting the oxysterol-binding protein. *Cell Reports.* 10:600–615. https://doi.org/10.1016/j.celrep.2014.12.054

Uchida, Y., J. Hasegawa, D. Chinnapen, T. Inoue, S. Okazaki, R. Kato, S. Wakatsuki, R. Misaki, M. Koike, Y. Uchiyama, et al. 2011. Intracellular phosphatidylserine is essential for retrograde membrane traffic through endosomes. *Proc. Natl. Acad. Sci. USA.* 108:15846–15851. https://doi.org/10.1073/pnas.1109101108

Várnai, P., B. Tóth, D.J. Tóth, L. Hunyady, and T. Balla. 2007. Visualization and manipulation of plasma membrane-endoplasmic reticulum contact sites indicates the presence of additional molecular components within the STIM1-Orai1 Complex. *J. Biol. Chem.* 282:29678–29690. https://doi.org/10.1074/jbc.M704339200

Venditti, R., M.C. Masone, L.R. Rega, G. Di Tullio, M. Santoro, E. Polishchuk, I. Castello Serrano, V.M. Olkkonen, A. Harada, D.L. Medina, et al. 2019. The activity of Sac1 across ER–TGN contact sites requires the four-phosphate-adaptor-protein-1. *J. Cell Biol.* https://doi.org/10.1083/jcb.201812021

Weber-Boyvat, M., H. Kentala, J. Peränen, and V.M. Olkkonen. 2015. Ligand-dependent localization and function of ORP-VAP complexes at membrane contact sites. *Cell. Mol. Life Sci.* 72:1967–1987. https://doi.org/10.1007/s00018-014-1786-x

Yeung, T., G.E. Gilbert, J. Shi, J. Silvius, A. Kapus, and S. Grinstein. 2008. Membrane phosphatidylserine regulates surface charge and protein localization. *Science.* 319:210–213. https://doi.org/10.1126/science.1152066